Super-resolution microscopy of alpha-synuclein aggregates in brain samples indicates a subset of cells have disrupted protein homeostasis

Emre Fertan[1,2,3*,✤], John S. H. Danial[1,2,4*,✤], Stephen Neame[5], Georg Meisl[1,2], Jeff Y. L. Lam[1,2,6*], Melanie Burke[1,2], Zengjie Xia[1,2,7*], Yunzhao Wu[1,2], Ben Powney[5], Yoichi Imaizumi[5], Annelies Quaegebeur[3], James Staddon[5], David Klenerman[1,2,✉]

[1]Yusuf Hamied Department of Chemistry, University of Cambridge, Cambridge, UK CB2 1EW.
[2]UK Dementia Research Institute at University of Cambridge, Cambridge, UK CB2 0XY.
[3]Department of Clinical Neurosciences, University of Cambridge, Cambridge, UK CB2 0XY.
[4]School of Physics and Astronomy, North Haugh, University of St Andrews, UK KY16 9SS.
[5]Eisai Ltd., EMEA Knowledge Centre, Mosquito Way, Hatfield, UK AL10 9SN.
[6]Division of Life Science, The Hong Kong University of Science and Technology, Clear Water Bay, Kowloon, Hong Kong.
[7]UK Dementia Research Institute at University College London, London, UK WC1E 6BT.
✤Co-first authors.
*Current affiliation.

✉ **Correspondence to:** Professor Sir David Klenerman, Yusuf Hamied Department of Chemistry, University of Cambridge, UK, CB2 1EW, dk10012@cam.ac.uk

Manuscript: 27 pages, 9 figures, 6 supplemental figures, 1 table.

Running title: Morphology of alpha-synuclein aggregates.

Conflict of interest: Authors declare no conflict of interest.

Abstract

Small-soluble aggregates of alpha-synuclein has been observed in Parkinson's disease (PD). However, the processes that occur *in-vivo* leading to the formation of these aggregates are not well understood. We used sensitive single-molecule methods including SIMOA and super-resolution microscopy to quantify and characterise alpha-synuclein aggregates harvested from human brain samples alongside the Line 61 mouse model using different tissue processing methods. Different sub-populations of aggregates were accessible by different extraction methods and larger aggregates were detected in older mice and PD brain, although the aggregate number did not change significantly in younger mice and controls, respectively. In the mice there was a substantial population of larger (150 nm), fibrillar aggregates, while in PD this population of larger aggregates (100 nm) was only slightly greater than the controls. Our data suggests that alpha-synuclein aggregates slowly in the brain, leading to formation of larger aggregates in a sub-set of cells.

Keywords: Single-molecule detection, DNA-PAINT, soluble aggregate, Triton-X100, sarkosyl, extraction, data modelling

1. Background:

Affecting 4% of the population above the age of 80, Parkinson's disease (PD) is the second most common neurodegenerative disorder(1). With motor symptoms of rigidity, bradykinesia, and resting tremor(2), accompanied by speech dysfunction(3) -and in some cases cognitive impairment(4), PD significantly decreases the quality of life(5) and shortens the lifespan(6). While the exact cause(s) and neuropathological mechanisms of PD are still being studied, the loss of dopaminergic neurons in the substantia nigra pars compacta(7) as well as the aggregation and accumulation of alpha-synuclein (αSyn)(8,9) have been well documented.

As a synaptic protein, αSyn is required for neurotransmitter release by aiding the formation of the soluble N-ethylmaleimide-sensitive factor attachment protein receptor (SNARE) complex(10). However, oligomeric αSyn species formed by the pathological aggregation of αSyn inhibit neurotransmitter vesicle docking and release(11,12). If the aggregation continues or the cell is stressed, αSyn can relocate from the synapse to the soma and promote neuronal toxicity(13). While the insoluble Lewy bodies are the most widely studied form of αSyn accumulation, recent studies have shown that the earlier forms of aggregation, namely the small-diffusible aggregates -which are highly heterogeneous in size and shape(14), may be more toxic than the Lewy bodies(15). Our group has recently shown that these diffusible αSyn aggregates are present in the amygdala of the brains of PD patients and, notably brains from unaffected individuals, but the diffusible aggregates differ in size between PD and control cases, and the aggregates under 200 nm in length are neurotoxic(16).

Various mouse models have been engineered to study αSyn aggregation and its link to PD pathology. The Line 61 model was first developed and described by Rockenstein *et al.*(17), as a X chromosome-linked knock-in model, expressing human *SNCA* gene under the murine thymocyte differentiation antigen 1 (Thy1) promoter in C57BL/6xDBA/2 mice(18). Unlike many mouse models over-expressing disease-associated proteins at unphysiologically high levels, the Line 61 mice express full-length human αSyn at moderate levels throughout the brain. Histopathological and Western blot analysis showed a 1.5- to 3.4-fold rise in expression(19), which is comparable to individuals with familial PD due to *SNCA* gene triplication(20). While αSyn accumulation starts around 1 month of age, no significant dopaminergic or motor neuron loss has been reported, even at advanced ages(17,19). On the other hand, hippocampal neuronal loss -especially in the CA3, is apparent by 3 months of

age(21) and deficits in dopamine release and striatal pathology, along with increased gliosis (both astrocytes and microglia), and mitochondrial dysfunction are observed by 6-months of age(22–25). Motor and non-motor behavioural dysfunction has also been reported in this model, starting as early as 1-month and progressing with age(19,26).

While brains from PD patients and model systems such as the Line 61 mice have been histopathologically characterised at a microscopic level, the small-diffusible αSyn aggregates have not been comprehensively characterised and compared between humans with PD and the model systems. As outlined above, these smaller aggregates may be more heavily involved in PD pathogenesis, making it essential to characterise them, in order to both better characterise the behaviour of the mouse model and gain insight on PD pathogenesis. However, this is a challenging task for two reasons. Firstly, the small-diffusible aggregates are highly heterogenous, low in abundance, and below the diffraction-limit of light, making them invisible to traditional microscopy techniques and bulk analysis methods. Single-molecule and super-resolution detection methods are required to resolve individual aggregates, so they can be quantified and characterised. Moreover, the methods used to process the brain tissue and harvest the aggregates often yield a subset of the aggregates present in the tissue and may alter their properties and size distribution. This can bias observations towards the species which are dominant for a particular extraction method. For instance, Hong *et al.*(27) demonstrated that the method used to process post-mortem Alzheimer's disease brain samples impacts the type of beta-amyloid aggregates collected: while lysing the cells by breaking the cell membrane with detergents and mechanical agitation yielded a higher number of aggregates, gently soaking the samples gathered a small subsection of the aggregates(28) that are capable of inducing long-term potentiation deficits(27,29). On the other hand, more rigorous tissue extraction methods employing detergents such as Triton X-100 (TrX) and N-laurylsarcosine (sarkosyl) are also used in various protocols to harvest and study protein aggregates that are not released by other methods. Using TrX extraction, Hyman and colleagues showed an increase in insoluble αSyn levels in dementia with Lewy body (DLB) patients, while the quantity of TrX soluble aggregates did not differ(30). Meanwhile, sarkosyl is a stronger detergent, used to solubilise protein aggregates that otherwise remain insoluble(31). It has previously been shown that sarkosyl can solubilise αSyn fibrils from human post-mortem PD brain samples(32).

Due to the issues discussed above, the morphology of the small-diffusible αSyn aggregates produced in mouse models and their similarity to human PD brain-derived

aggregates remains elusive, thus the degree to which these mouse models are useful in the study of αSyn aggregation has remained challenging to determine. In order to address these issues, we use single-molecule detection and super-resolution microscopy to determine the size and shape of the αSyn aggregates from the brains of Line 61 mouse model of PD as well as post-mortem human brain samples. We compare gentle tissue soaking and homogenising with artificial cerebrospinal fluid (aCSF), then TrX, and sarkosyl tissue extraction methods (**Figure 1**). This information on the number and size distribution of the αSyn aggregates can be modelled by a chemical kinetics approach to gain new insights into the aggregation of αSyn in vivo in both mice and humans.

2. Methods:

2.1 Mouse tissue collection and sample preparation: Due to the appearance of αSyn accumulation by 1-month and the pathophysiological symptoms by 6-months of age, and the age-related symptom progression, 1.5-, 6-, 9-, and 12-month-old mouse brains were used in this study, acquired from QPS (now Scantox Neuro). Brains were harvested from a total of 24 male Line 61 (6 mice per group at 1.5-, 6-, 9- and 12-months of age), following euthanasia with sodium phenobarbital (200 mg/kg) and perfusion with phosphate buffered saline (PBS 10%). 12 of the brains were used for the gentle soaking extraction (**Figure 1a**), while the remaining 12 were powdered (homogenised) and serial extractions with artificial cerebrospinal fluid (aCSF), TrX, and sarkosyl were performed (**Figure 1b**).

For the gentle soaking protocol, mouse cerebral tissue was first cut down into small pieces with a scalpel and transferred to 1.5 mL lo-binding Eppendorf tubes. 600 µL of aCSF buffer (bio-techne TORIS, Cat. 3525) containing 150 nM Na^+, 3 nM K^+, 1.4 nM Ca_2^+, 0.8 nM Mg_2^+, 1 nM P and 155 nM Cl^- with Halt™ protease and phosphatase inhibitor single-use cocktail (100x; Thermo Fischer Scientific, Cat. 78442) was added to each sample and incubated for 45-minutes at 4°C on a HulaMixer™. Then the samples were centrifuged at $17{,}000_x$g for 120-minutes at 4°C, the supernatant was collected and stored in a -80°C freezer until analysis.

For the serial extractions, the intact mouse cerebrum was first frozen with liquid nitrogen and grounded into powder using a mortar and pestle. Then the powder was transferred into a 1.5 mL lo-binding Eppendorf tube and the initial aCSF extraction was performed as described above. The supernatant (homogenised/powder sample) was collected and stored at -

80°C until analysis. Meanwhile, the centrifugation pellet was resuspended with 500 µL aCSF containing inhibitors as described above, as well as 1% (by volume) TrX (Fischer Scientific, Cat. 11488696) and incubated for 45-minutes at 4°C on a HulaMixer™. Then the samples were centrifuged at 17,000$_x$g for 120-minutes at 4°C, the supernatant (TrX soluble sample) was collected and stored in a -80°C freezer until analysis. Then the centrifugation pellet was once again resuspended with 500 µL aCSF containing inhibitors as described above, as well as 1% (by volume) sarkosyl (Sigma-Aldrich, Cat. 61747-100ML) and the same extraction described above was performed to acquire the sarkosyl soluble sample.

2.2 Human tissue collection and sample preparation: Due to the low availability of post-mortem human brain tissue, a slightly different protocol was followed: 3 PD and 3 age- and sex-matched (two female, one male) post-mortem orbitofrontal cortex (Brodmann areas 10-11) samples were first dissected into 300-350 mg pieces (**Table 1**). Then the initial aCSF soaking extraction was performed as described for the mouse tissue above. Following the soaking extraction, the remaining tissue was homogenised by first adding 1 mm zirconium beads (Scientific Labs, Cat. SLS1414) and 500 µL aCSF with protease/phosphatase inhibitors and processing the samples on an electronic tissue homogeniser (VelociRuptor V2 Microtube Homogeniser, Scientific Labs, Cat. SLS1401), at 5 meters/sec for 2 cycles of 15 seconds, with a 10 second gap in between, followed by centrifugation at 17,000$_x$g for 120-minutes at 4°C. Then further extractions were performed with TrX and sarkosyl, as described above (**Figure 1c**).

2.3 BCA assay: Total protein concentration in the samples processed by different methods was determined using a bicinchoninic acid (BCA) assay (**Figure 1d**; Pierce™ BCA Protein Assay Kit, Thermo Fischer Scientific, Cat. 23227). In brief, samples (1:5 by volume) were diluted in PBS and 25 µl diluted sample was loaded in duplicates into a 96-well plate. Bovine serum albumin (BSA) assay standards were also diluted in PBS at instructed amounts by the kit and loaded alongside the samples, also at 25 µl. Assay working reagent was prepared by mixing 50 parts of BCA Reagent A with 1 part of BCA Reagent B (50:1, Reagent A:B), provided with the kit and added at 200 µl to each sample. The plate was gently shaken for 30 seconds, covered, and incubated at room temperature for 30 minutes. Then the absorbance was measured at 562 nm on a plate reader.

2.4 SiMoA assay: αSyn aggregates in the mouse and human brain samples were quantified using single-molecule array (SiMoA; **Figure 1e**). SiMoA® Homebrew carboxylated beads (Quanterix; Cat.104006) were first functionalised with monoclonal 4B12 antibody (Thermo Fisher Scientific; Cat. MA1-90346) as described in the Quanterix Homebrew instruction manual. In brief, antibodies were buffer-exchanged with the provided bead conjugation buffer and 1 mL of the paramagnetic carboxylated beads (4.2×108 beads) were washed with the provided bead wash buffer followed by the bead conjugation buffer with the. 9 µL of EDC solution was added to the washed beads and the reaction mixture was incubated on a mixer for 30 minutes at 4°C. After washing the activated beads once with cold 25 mM MES, the buffer-changed antibodies (0.2 mg/mL, 300 µL) were added. The reaction mixture was incubated on a mixer at 4°C for two hours. The conjugated beads were then washed with the provided bead wash buffer and blocked with the blocking buffer at room temperature for 40 minutes.

The beads coated with the 4B12 antibody were first washed three times with the provided bead diluent in the kit. Meanwhile, to each well on a conical bottom microplate (Quanterix), conditioned media samples were diluted with the lysate sample diluent (2:98) to give 100 µL solution at the desired concentration. Then, 25 µL of the washed beads were introduced to each well to give the final-bead concentration as 2×10^7 beads/mL. The samples and the beads were incubated on the plate shaker at 30°C at 800 rpm for 30 minutes. The plate was then washed by the SiMoA washer with the provided buffers. Then, the biotinylated detector antibody 4B12 was diluted to 0.1 µg/mL with the provided Homebrew detector diluent and 100 µL of the diluted detectors were introduced to each well. The mixture was then incubated on the plate shaker at 30°C with 800 rpm for 10 minutes. Similarly, the plate was then washed by the SiMoA washer. Meanwhile, the provided streptavidin-β-galactosidase (SBG) concentrate was diluted to 50 pM with SBG diluent. 100 µL of the diluted SBG was added to each well and the mixture was incubated on the plate shaker at 25°C at 800 rpm for 10 minutes. Finally, the plate was washed by the SiMoA washer and loaded onto the SR-X™ Biomarker Detection System (Quanterix) together with the SiMoA disc, tips, and an equilibrated, well-shaken and opened RGP bottle.

2.5 DNA-PAINT with SiMPull imaging: αSyn aggregates in the mouse and human brain samples were characterised in terms of their size and shape using DNA point accumulation in nanoscale topography (DNA-PAINT) microscopy combined with single-molecule pulldown (SiMPull)(33). SiMPull coverslips were prepared as described previously(16,33) and kept in

vacuumed containers at -20°C until used. At the beginning of each experiment, one vacuum box containing the coverslips was taken out of the freezer and placed inside a fume-hood to allow equalisation of the temperature. The coverslip was first coated with neutravidin (0.2 mg/mL) diluted in TBST(v/v) (0.05% Tween 20 Cat. P1379-25ML diluted in tris-buffered saline (TBS)) for 10-minutes. After removing the neutravidin solution, each well was washed with TBST (two cycles) and then with TBS with 1% Tween (one cycle)-hereon described as washing. Biotinylated 4B12 antibody was diluted to 10 nM in TBS containing 0.1 mg/ml bovine serum albumin (BSA; Thermo Scientific; Cat. 10829410) and incubated for 15 minutes. Then the wells were washed, and samples were incubated overnight at 4°C. While the cut, powder, and sarkosyl extracted samples were tested neat, the TrX extracted sample was diluted in TBS 50:50 by volume. In order to minimise non-specific binding, a blocking step was performed after samples incubation, with solution containing 3 mg/ml BSA in TBS, incubated for 30 minutes. Then the DNA-labelled 4B12 antibody diluted to 2 nM in TBS containing 0.1 mg/ml bovine serum albumin was incubated for 30 minutes (labelling protocol explained by Fertan et al., 2023(33)). After the washing steps, TetraSpeck microspheres (1:7,000 in TBS, 10 µL, Thermo Scientific; Cat. T7279) were introduced to each well for 10 minutes. The TetraSpeck solution was then removed, followed by a single wash with TBST, and a second PDMS gasket (Merck, GBL-103250-10EA) was stacked on the coverslip before introducing 4 µL of imaging strand (TGGTGGT- cy3B; atdbio) in TBS. Finally, the coverslip was sealed with another coverslip on top of the second PDMS gasket (**Figure 1f**). The coverslip was imaged using a purpose built total internal reflection fluorescence (TIRF) microscope(34) using a 568-nm (green) excitation laser for 4,000 per field of view (FoV) at an exposure time of 100 ms (**Figure 1g**). As measured previously(34), the spatial resolution of this setup is ~30 nm's. Aggregates below this length were not included in the analyses.

<u>2.6 Data analyses:</u> All BCA and SiMoA assays were run in duplicates and the data were averaged. DNA-PAINT imaging was performed for 4 FoV's per well and two wells for each sample, from which the data were pooled. Super-resolution images were reconstructed, drift corrected, and analysed using a software developed by our group(35). The R Project Statistical Computing version 4.2.2 (2022-10-31)—" Innocent and Trusting" was used for all statistical analyses, the graphs were generated in GraphPad Prism 7.0a for Mac OS X and Inkscape, and the cartoon figures were created with BioRender.com. Linear mixed effects models, ANOVA's with Type 2 sums of squares, and Welch Two Sample t-tests were used to determine differences between the groups and corresponding 95% confidence intervals (CI) were reported. The

datasets generated and analysed during the current study are available from the corresponding author on reasonable request.

2.7 Distribution fitting: Models of the aggregate length distribution have been derived for controlled conditions of purified protein aggregating at a constant free monomer concentration(36). It assumes that aggregates grow into linear structures by addition of monomeric proteins to their ends and can fragment at any place along the fibril with equal probability. The theoretical size distributions are effectively determined by a single parameter, the average length, $\sqrt{\xi}$. The distribution is given by

$$\rho(j) = \frac{e^{-\frac{2(j-nc)(2\sqrt{\xi}+j+nc)}{1+4\xi}}\left(4j\left(2\sqrt{\xi}+j\right)-1\right)}{(1+4\xi)(\sqrt{\xi}+nc)}$$

where $\xi = \frac{2k_+m_0}{k_-}$, j is the length in terms of monomers, n_c is the nucleus size, k_+ is the elongation rate constant, k_- is the fragmentation rate constant and m_0 is the monomer concentration. The sum of 2 distributions used to fit the data is then

$$A_1\rho(j,\xi_1) + A_2\rho(j,\xi_2)$$

To fit the experimental data, we used a cutoff at 40nm (anything below this value cannot be sized accurately, due to the intrinsic size of the label). Fitting was performed by binning experimental data into 10nm bins and using least squares to fit the data above the cutoff to equation (2), with 4 free fitting parameters, the magnitude of the two distributions, A_1 and A_2, and their means, ξ_1 and ξ_2. **Figure 9** shows ξ_2 and the relative contribution of distribution 2, $A_2/(A_1+A_2)$.

3. Results:

The small, αSyn aggregates studied here are mostly below the diffraction-limit of light (~200 nm), thus invisible to traditional light microscopy techniques such as immunohistochemistry. Moreover, their high heterogeneity and low abundance makes it difficult to separate the disease-relevant species from the larger aggregates and monomers with bulk analysis methods such as ELISA. As such, single-molecule detection methods are required to quantify and morphologically characterise these aggregates individually with high precision, and to compare them between different tissue sources and extraction methods. Here, we used an ultra-sensitive single molecule array (SiMoA) assay developed by our group to quantify αSyn aggregates specifically (excluding monomers) in the samples, with femtomolar

sensitivity(37). Then, the aggregates were characterised in terms of their size and shape, using a combination of single-molecule pulldown (SiMPull) and DNA-PAINT imaging, previously developed and used by our group to characterise beta-amyloid(33) and tau aggregates(38). Since the same monoclonal antibody is used to capture and detect the targets, only aggregates are studied, excluding the monomeric αSyn in the samples. Moreover, the total number of localisations (imaging strands bound to the aggregates) can be calculated, positively correlating with the total target mass in the sample(39). The results of these experiments are presented below, and the full results of statistical tests (including degrees of freedom, p-values, and CI's) are provided in the **supplemental results file**.

3.1 αSyn aggregate concentration in Line 61 mouse brain: First, we used an ultra-sensitive SiMoA assay to quantify the αSyn aggregate concentration in the 1.5-, 6-, 9-, and 12-month-old Line 61 mouse brain samples extracted by gentle soaking (cut), homogenising (from powdered tissue), TrX, and sarkosyl. While the αSyn aggregate quantity did not differ between the ages (**Figures 2a-d**), concentration of aggregates harvested by homogenising, TrX, and sarkosyl extractions differed significantly. The highest concentration of αSyn aggregates was found in the homogenised samples, followed by the TrX soluble extract, and least amount of aggregates was in the sarkosyl soluble fraction (**Figures 2e-h**). Meanwhile, the soaked samples, which were prepared from a different brain sample contained a smaller amount of aggregates, compared to the other extraction methods.

3.2 Extraction methods affect aggregate morphology: Following quantification, we further characterised the αSyn aggregates in terms of their size and shape, using super-resolution DNA-PAINT microscopy (**see Figure 8 for sample images**). For the soaked samples, the average aggregate length was 100 nm at 1.5-months of age and increased to 114 and 123 nm by 6- and 9-months of age but decreased to an average of 74 nm at 12-months of age, suggesting a change in the morphology of soaked aggregates as the Line 61 mice age (**Figures 3a&e and Figure 4a**). Aggregate area from the soaked samples followed a similar trend, with an increase at 9-months of age, followed by a decrease at 12-months (**Figures 3a&i and Figure 4e**). Meanwhile, aggregate eccentricity (which is a measure of aggregate shape, with values close to 0 representing circular aggregates and values close to 1 representing more cylindrical aggregates) did not change with age and had a value close to 1, indicating the presence of more fibrillar aggregates in all samples (**Figures 3a&m and Figure 4i**). Within the serially extracted samples, the homogenised and TrX soluble aggregates had an average length of 128 and 142

nm respectively, and thus were longer than the sarkosyl soluble aggregates, which had an average length of 59 nm. However, while the TrX soluble aggregates steadily grew longer as the mice aged, the homogenised aggregates varied in length but showed no clear trend with age. In contrast, while the sarkosyl soluble aggregates grew longer after 1.5-months of age, they did not show any further significant age-related changes in length (**Figures 3b-d&f-h and Figures 4b-d**). The area of the TrX soluble aggregates grew larger with age, while homogenised and sarkosyl soluble samples had a fluctuating pattern (**Figures 3b-d&j-l and Figures 4f-h**). On the other hand, eccentricity of the serially extracted samples differed by extraction method. While the homogenised and TrX soluble aggregates were more fibrillar, the sarkosyl soluble aggregates were more circular (**Figures 3b-d&n-p and Figure 4j-l**).

Collectively, these results show that the initial homogenising and extraction with aCSF does not harvest all the αSyn present in the cerebrum of the Line 61 mice and further extractions with detergents obtain aggregates not accessible by detergent-free homogenising. Importantly, these detergent-soluble aggregates differ from the aCSF soluble aggregates in size and shape. Moreover, while the total aggregate concentration estimated using the number of localisations did not change with age (**Figure 5a**), older Line 61 mice formed larger aggregates -mostly in the TrX and sarkosyl soluble fragments, leading to a higher total mass of aggregated αSyn after 6-months of age (**Figure 5b**).

<u>3.3 αSyn aggregate concentration in PD and control brain:</u> Following the Line 61 transgenic mouse model of PD, we processed age- and sex-matched PD and control post-mortem human orbito-frontal cortex samples with serial extractions and compared the quantity as well as the morphology of the αSyn aggregates (**see Figure 8 for sample images**). While the αSyn aggregate quantity did not differ between the PD brains and the control samples (**Figure 5c**), there was a significant difference between aggregates obtained using the different extraction methods (**Figures 5d & 6)**. The sarkosyl soluble fraction contained the least number of aggregates for both phenotypes, followed by the soaked and TrX extracted fractions, and the homogenised fragments contained the highest concentration of αSyn aggregates.

<u>3.4 PD brains contain larger aggregates than controls:</u> Although the number of aggregates did not differ between the PD and control brains, the morphology of the aggregates differed significantly, as the PD brains contained longer (80 vs 65 nm) and larger (1360 vs 770 nm^2) aggregates, with rounder (less fibrillar) shapes, regardless of extraction method, leading to

higher total mass of aggregated αSyn in the PD brains (**Figure 5d**). For the control brains, the longest (74 and 70 nm; **Figure 7a**), largest (1140 and 835 nm^2; **Figure 7d**), and roundest (eccentricity 0.83 and 0.83; **Figure 7g**) aggregates were harvested by homogenising and by sarkosyl extraction. On the other hand, for the PD samples, the homogenised and TrX extracted aggregates were longer (93 and 90 nm; **Figure 7b**) and larger (1980 and 1490 nm^2; **Figure 7e**), while the shortest (63 nm) and smallest (950 nm^2) aggregates were in the sarkosyl extracted samples. Unlike the control brains, the larger aggregates were more fibrillar in the PD brain, as the aggregates with the highest eccentricity were found in the homogenised fraction, followed by the TrX extraction, and the roundest aggregates were in the sarkosyl soluble fraction (**Figure 7h**).

3.5 Comparing PD human and transgenic mouse aggregates: An essential question in the field of dementia research and in the broader field of neuroscience is the validity of animal models. Since the morphology of pathological aggregates is related to their toxic properties(16,40), an important requirement of a useful mouse model for studying disease pathogenesis and testing novel therapeutics is likely to be that the aggregates formed are similar to the ones in humans. In order to evaluate the Line 61 mouse model of PD in terms of its aggregate validity, we compared the size and shape of the αSyn aggregates from the 12-month-old mouse cerebrums and human PD brain samples.

Regardless of the extraction method, there were significant differences in aggregate length, area, and eccentricity between the αSyn aggregates from Line 61 and human post-mortem PD brains. While the aggregates in the Line 61 mice were longer, smaller, and more fibrillar, the aggregates found in the human brain were shorter, larger, and rounder. The homogenised and TrX soluble fractions contained the longest aggregates in both species and the sarkosyl soluble fragment had the shortest aggregates. Interestingly, the species difference was also greater for the homogenised and TrX extracted fractions, as the aggregates from the mice were considerably longer than the human aggregates for these samples, while the sarkosyl soluble aggregates differed less and in the opposite direction (**Figures 7b-c**). Meanwhile, the opposite trend was present for aggregate area: while the homogenised and TrX extracted fractions contained the largest αSyn aggregates regardless of species, the aggregates within these samples from the human brain were significantly larger. Similarly, the soaked aggregates from the human brain were also larger than the ones from the Line 61 mice (**Figures 7e-f**). While the homogenised and TrX extracted fractions were more fibrillar for both mice and

humans, the difference was greater for the Line 61 mice, which had higher eccentricity values, explaining the longer but smaller aggregates compared to the human aggregates in those extraction methods (**Figures 7h-i**).

4. Discussion:

In this study, we quantified and characterised αSyn aggregates from brains of the Line 61 mouse model over-expressing human αSyn at four different ages and human post-mortem brain samples from PD patients and age/sex matched unaffected controls. We processed the tissue using serial extractions with four commonly used methods to harvest diffusible aggregates. As such, we were able to address five questions: (1) does the quantity or morphology of the αSyn aggregates change as the Line 61 mice age?; (2) do different extraction methods harvest different types of aggregates in mouse and human samples?; (3) how do the αSyn aggregates from a mouse model compare to human samples?; (4) how do the αSyn aggregates from post-mortem PD brain samples compare to controls?; (5) can the aggregate size distribution be fitted by chemical kinetics and what does this reveal about the aggregation of αSyn *in-vivo*?

4.1 Age-related changes in αSyn aggregates in Line 61 mice: Histopathological αSyn accumulation starts in the Line 61 mice by 1-month of age(19). As demonstrated by Rabl *et al.*,(26) while the total (monomeric and aggregate) TrX soluble human αSyn levels increase until 6-months of age in the hippocampus, they decrease in the striatum. On the other hand, the TrX insoluble fragments does not change significantly in either region(26). By different methods, our results show that the number of aggregates does not change over time (as measured by SiMoA), yet their size increases with age (measured by DNA-PAINT), leading to greater total αSyn mass in the brains of older mice. As such, the constant presence and slow growth of the αSyn aggregates may eventually lead to PD-like pathology. However, this age-dependent increase in aggregate size was not detectable with all extraction methods; while the aggregates in the homogenised and TrX soluble fragments grew larger by 12-months of age, the aggregates in the soaked samples got smaller. This harvesting method-dependent difference in aggregate morphology demonstrates the presence of aggregates accessible by different methods in the brain tissue and highlights the importance of studying the relationship between the harvesting method and the aggregates collected.

4.2 Comparing different tissue processing methods: We found significant differences between the extraction methods in terms of aggregate concentration and morphology, both in mouse and human samples. While the soaked samples contained a lower concentration of aggregates in the mice, the highest concentration was in the detergent-free homogenised samples, followed by TrX and sarkosyl extractions. In the human samples, lower amounts were measured in the sarkosyl soluble fractions, followed by soaked, TrX extracted, and homogenised. These results are in parallel with Walsh and colleagues(27), as they showed a small portion of more toxic, readily diffusible Aβ aggregates in soaked AD brain samples. Importantly, TrX and sarkosyl extraction further harvested αSyn aggregates during the serial extraction process, showing that homogenising the brain tissue (and then the TrX extraction) does not release all the αSyn aggregates.

Importantly, both in mouse and human PD samples, the size and shape of the aggregates differed between the extraction methods. The homogenised and TrX extracted samples were larger than soaked and sarkosyl soluble samples, indicating the presence of larger species after the initial homogenised extraction, which can be mostly harvested by TrX, leaving behind aggregates, which either entirely or partially made soluble by sarkosyl. Since methods used to determine the structure of the aggregates, such as cryo-EM use specific tissue preparation methods (sarkosyl insoluble in the case of cryo-EM)(41), the species characterised by these methods may only be containing a small subsection of all aggregates produced by the patients and animal models. Similarly, different tissue processing methods used by laboratories for standard immunoassays may give rise to differing results.

4.3 αSyn aggregates produced by the Line 61 mice morphologically differ from ones found in the human brain: We also compared the αSyn aggregates from post-mortem human brain samples with the Line 61 mice. The Line 61 mice had a significantly higher (~10-fold) aggregate load compared to the humans, probably due to the over-expression of the *SNCA* gene. We have also found that the αSyn aggregates in the human brain are shorter with larger total areas, and rounder compared to the ones in the Line 61 mouse brain. While on average the human aggregates were shorter than 100 nm, agreeing with previous findings from our group(16), the aggregates in the mouse brain, especially the ones in the homogenised and TrX soluble fragments were about 150 nm in length. The presence of longer aggregates in the mice may be due to the over-expression of αSyn, meaning that the aggregate removal processes are

overwhelmed and resulting in more fibrillar aggregates than in human. Humans have less rapid aggregation and hence removal processes are more effective, so that less larger fibrillar aggregates form. Overall, the proportion of aggregates in the different fractions were remarkably similar between the humans and the Line 61, suggesting that the aggregate properties which determine the relative amounts in each fraction are similar in both animals and humans.

4.4 Size but no concentration difference for αSyn aggregates in human brains: The prefrontal cortex has extensive dopaminergic input and thus executive dysfunction is a major symptom of PD(42). Specifically the orbitofrontal cortex volume and pathology is linked to deficits in reward processing and decision making(43,44). Due to this functional and anatomical connectivity between the dopaminergic midbrain and the prefrontal cortex, here we studied samples from the orbitofrontal cortex, at Braak stage 4 and 5, during which the Lewy pathology is well observed in the substantia nigra, but not yet as prevalent in the neocortex(45). This stage was selected as it is hypothesised that the small-diffusible aggregates precede the Lewy bodies and thus their presence in the orbitofrontal cortex can be beneficial to understand the αSyn aggregation prior to significant neuronal loss(46) during the pathogenesis of PD.

While the aggregate numbers did not differ between PD brains and controls, PD samples contained larger and more spherical aggregates leading to a higher total aggregate mass, indicating that there has been disruption of protein homeostasis and hence increased aggregation. However, if all the neurons showed increased aggregation, then one would expect an increase in aggregate concentration along with an increase in average aggregate size. However, if only a small fraction of neurons or just some part of the neuron has disrupted protein homeostasis leading to growth of longer aggregates, this could result in an increase in an average length but no change in aggregate concentration. This is what we observed in this study, indicating the presence of multiple cell populations at different stages of PD phenotype. It is worth noting that in any experiment on post-mortem brain, it is only the neurons that were alive at the end of life that are studied. This means that if increased αSyn aggregation ultimately results in cell death, then these aggregates would be released into the extracellular space and not detected in these experiments. This survival-bias leads to a smaller difference between the aggregates in PD and control brain.

Our previous work imaged the aggregates in the soaked fraction in the amygdala, which unlike the orbitofrontal cortex shows high levels of neuronal loss at this stage(47). This study used a different super-resolution method based on an aptamer that imaged beta-sheet containing aggregates (ie. both fibrillar beta-amyloid and αSyn)[16], thus the results cannot be directly compared with the current study. Nevertheless, it is noteworthy that we have shown smaller aggregates in the PD samples compared to the controls, suggesting that prior to neuronal loss, larger αSyn aggregates form (as seen in the orbitofrontal cortex), which then possibly leads to the loss of the neurons containing these larger aggregates, leaving the cells with smaller aggregates behind. Moreover, the observation that the soaked fraction from PD brain was more inflammatory than fraction from control brain is consistent with the aggregates in PD brain being more cytotoxic. This also highlights that in future work it will be informative to compare the aggregates in different brain regions at different disease stages using the same imaging method, as PD pathology seems to progress at different rates in different brain regions, with the formation of larger aggregates leading to cell death and related behavioral phenotypes.

<u>4.5 Biophysical models of the aggregate length distributions imply two aggregate populations:</u> We have previously used a chemical kinetic approach to model protein aggregation *in-vitro* (test tube) and *in-vivo*(48–50). This model includes nucleation, linear aggregate growth by elongation, and aggregate replication by fragmentation. Using this model, it is possible to derive an expression for the expected size distribution of aggregates. However, although this description is able to accurately model length distributions measured during the aggregation of purified proteins *in-vitro*, it is not obvious that the shape of the distribution will be maintained *in-vivo*, where other factors, in particular aggregate removal and heterogeneity of pathology may affect the size distribution. In the present dataset, we found a clear deviation from the theoretical distribution of a simple “linear growth with fragmentation” model (**Supplemental Figures 1&2**). While this inability of our simple model to describe the *in-vivo* length distributions may indicate that additional processes to growth and fragmentation are also taking place, another aspect of *in-vivo* data affects the measurements: the length distributions measured here from the soaked, homogenized, TrX, and sarkosyl treated samples contain pooled contributions from many different cells with unequal disease phenotypes. Conditions for aggregation may differ in these cells, leading to the overall distribution being a weighted average of many individual distributions of individual cells. Indeed, histopathological studies indicate that there may be a large population of homeostatic cells and a small population of cells with large amounts of aggregates(51). We therefore proposed the following minimal

model that assumes two different populations of cells: the overall aggregate population is the weighted sum of two aggregate length distributions, each being described by our minimal model that matches *in-vitro* data. We thus fitted the experimental length distributions to this sum of two length distributions (**Figures 9a&b**). The resulting distribution, which contains relative contributions from populations of shorter and longer αSyn aggregates can describe most of the human data accurately (**Figures 9b-d**). These data are thus consistent with the presence of cells with PD phenotype and healthier ones in the human brain, as shown previously using cell culture studies with Math2-expressing neurons in the hippocampal Cornu ammonis being highly susceptible to pathological seeding with pre-formed fibrils while neurons from the dentate gyrus were relatively spared(52). In these experiments cells with higher αSyn expression were more likely to form aggregates when seeded and if detectable aggregates formed the cells died, agreeing with our predictions based on the data collected in current experiment.

Remarkably, the distribution of shorter aggregates appears not to differ between PD and control samples, but in PD the distribution of longer aggregates is both shifted to longer aggregate lengths and contributes more to the overall distribution than in control samples. This indicates that the disease-associated aggregates are captured predominantly by this second, larger distribution. Moreover, the difference between the two populations for the PD and control samples is most prominent in the soaked samples, showing that even though this fraction contains a small portion of the aggregates harvested, they may be the most disease relevant ones, in-line with the findings of Walsh and colleagues in the AD brain(27). Despite these remarkable fits of the data and our expectations, it is important to keep in mind that this is a minimal model, which assumes linear aggregate formation and does not account for active removal processes, and only constitutes one possible explanation for the observed distributions. Meanwhile, some of the mouse data are not well captured by the modelled distribution shapes (**Figures 9a,e,f and Supplemental Figures 3-6**). This may be because processes which are not modelled play a more important role in the mouse. However, the fact that the model fits the human but not the mouse data well highlights that it is not a generic model that can simply fit any size distribution.

<u>4.6 Insights into the aggregation mechanism *in-vivo*:</u> It is remarkable that a simple two population aggregate model can fit the *in-vivo* data from the human data suggesting that the *in-vivo* aggregation process is similar to the test-tube. However, longer and more fibrillar aggregates are formed in the mouse model, potentially due to the higher level of αSyn. In

addition, we do not observe changes in the aggregate concentration as the Line 61 mice age, suggesting that only a sub-population of neurons have disrupted protein homeostasis leading to the accumulation of larger aggregates. Histopathological studies done on the Line 61 mice(21) and the differences between our current data and previous work(16) suggest that PD progress at different rates within the brain in a region specific manner(53), with the formation of larger aggregates in different regions leading to neuronal loss. If this is correct, then studying the entire brain in the Line 61 mice combines the aggregates from both the effected and homeostatic regions and decreases the difference between transgenic and control mice. This sub-population of neurons with disrupted protein homeostasis is larger in the mouse model, and small in the human PD brain, but stays at a roughly constant number of cells over the course of the disease. If aggregation continued in this sub-population of neurons, then there would be a greater number of larger aggregates with time. In this case it would be expected that the proportion of larger aggregates would increase as the disease progresses. The fact that this does not occur in the mice, and there is only a small difference between human PD and control samples can be explained most simply by the increased aggregation resulting in neuronal death so that the aggregate population remains in steady state.

Alongside the PD brains, we also observed aggregates in the control brain, indicating that diffusible αSyn aggregates are not only produced in Parkinson's disease. This can be explained by the aggregates in healthy cells being removed as fast as they form so the aggregates do not increase in size. In contrast there are some neurons where the rate of production of aggregates is faster than the removal, which leads to the formation of larger aggregates. However, if the larger aggregates result in cell death as discussed above then there is no increase in proportion of larger aggregates with disease progression. At one time the fraction of neurons with larger aggregates is about 30-40% in PD compared to 20-30% in healthy controls, suggesting that it is the presence of this higher proportion of neurons with larger aggregates over longer time is what leads to PD pathogenesis.

We previously studied the aggregation of αSyn in the test-tube using single molecule Fluorescence energy transfer (FRET)(48,49) and showed that aSyn formed small aggregates rapidly and that these then underwent a slow structural conversion to more stable fibril-like aggregates that could then rapidly grow and eventually form fibrils. The converted aggregates were more cytotoxic to neurons through increased oxidative damage. The second population of larger aggregates that we detect in the human PD and mouse brain could be these converted

more toxic aggregates, explaining both why once formed they overwhelm the cellular removal processes and how they result in cell death. In the mouse brains, faster aggregation would result in the formation of a greater number of larger converted aggregates before cell death occurs. In addition, other work has shown that seeding of iPSC-derived neurons with αSyn fibrils leads to the formation of Lewy body-like structures and then cell death supporting the concept that increased aggregation of αSyn and formation of fibril-like aggregates is cytotoxic(54). This would also explain why the number of Lewy bodies is low in PD and does not increase with disease progression. These assumptions need to be tested in future studies and their implications investigated. Indeed, if they are supported by experimental findings, these assumptions can explain the challenges to develop cellular models of αSyn aggregation, since any neuron that develops larger aggregates will die and hence will no longer contribute to most measurements.

5. Conclusion:

Our results show that different populations of αSyn aggregates exist in different parts of the brain tissue as well as different sub-populations of neurons within a single region, which can be harvested using different methods. The super-resolution imaging of these aggregates shows that the diffusible aggregates in the soaked fractions may be the most disease relevant aggregates, although they make up a small portion of all the small aggregates, suggesting that reducing αSyn aggregation in neurons would be a viable therapeutic strategy for PD.

6. List of abbreviations:

αSyn	Alpha synuclein
aCSF	Artificial cerebrospinal fluid
DLB	Dementia with Lewy body
DNA-PAINT	DNA Point Accumulation in Nanoscale Topography
FRET	Fluorescence energy transfer
PD	Parkinson's disease
Sarkosyl	N-Laurylsacosine
SIMOA	Single-molecule array
SiMPull	Single-molecule pulldown
SNARE	Soluble N-ethylmaleimide-sensitive factor attachment protein receptor
TBS	Tris-buffered saline
Thy1	Thymocyte differentiation antigen 1
TIRF	Total internal reflection fluorescence
TrX	Triton X-100

7. Declarations:

Ethics approval and consent to participate: Human post-mortem brain tissue was acquired from the Cambridge Brain Bank (Cambridge University Hospitals). The Cambridge Brain Bank is supported by the NIHR Cambridge Biomedical Research Centre (NIHR203312). We gratefully acknowledge the participation of all our patient and control volunteers.

Consent for publication: Not applicable.

Availability of data and materials: Data collected during these experiments will be made available upon reasonable request from the corresponding author. No novel code was generated during data analysis.

Competing interests: None to declare.

Funding: The work was supported by the UK Dementia Research Institute (which receives its funding from UK DRI Ltd), the UK Medical Research Council, Alzheimer's Society and Alzheimer's Research UK (ARUK-PG2020A-009), ARUK-PG2020A-009, the Royal Society and a grant from Eisai. The views expressed are those of the authors and not necessarily those of the NHS, the NIHR or the Department of Health.

Author contributions: E.F. Conception and design, data collection and statistical analysis, manuscript writing. J.S.H.D. Conception and design, data collection and image analysis, manuscript editing. S.N. Conception and design, data collection, manuscript editing. G.M. Model building and data fitting. M.B., J.Y.L.L., Z.X., Y.W., B.P., Data collection, Y.I. Conception and design. A.Q. Human brain sample preparation and characterisation. J.S. Conception and design, manuscript editing. D.K. Conception and design, manuscript editing, overall supervision of the project.

Acknowledgments: We would like to thank Dr. Rohan T. Ranasinghe for his help during data collection.

8. References:

1. Simon DK, Tanner CM, Brundin P. Parkinson Disease Epidemiology, Pathology, Genetics and Pathophysiology. Clinics in geriatric medicine. 2020 Aug;36(1):1.

2. Xia R, Mao ZH. Progression of motor symptoms in Parkinson's disease. Neuroscience Bulletin. 2012 Aug;28(1):39.

3. Smith KM, Caplan DN. Communication impairment in Parkinson's disease: Impact of motor and cognitive symptoms on speech and language. Brain and language. 2018 Aug;185:38–46.

4. Cosgrove J, Alty JE, Jamieson S. Cognitive impairment in Parkinson's disease. Postgraduate medical journal. 2015 Aug;91(1074):212–20.

5. Zhao N, Yang Y, Zhang L, Zhang Q, Balbuena L, Ungvari GS, et al. Quality of life in Parkinson's disease: A systematic review and meta-analysis of comparative studies. CNS neuroscience & therapeutics. 2021 Aug;27(3):270–9.

6. Pinter B, Diem-Zangerl A, Wenning GK, Scherfler C, Oberaigner W, Seppi K, et al. Mortality in Parkinson's disease: a 38-year follow-up study. Movement disorders : official journal of the Movement Disorder Society. 2015 Aug;30(2):266–9.

7. Parent M, Parent A. Substantia nigra and Parkinson's disease: a brief history of their long and intimate relationship. The Canadian journal of neurological sciences Le journal canadien des sciences neurologiques. 2010 Aug;37(3):313–9.

8. Spillantini MG, Schmidt ML, Lee VMY, Trojanowski JQ, Jakes R, Goedert M. Alpha-synuclein in Lewy bodies. Nature. 1997;388(6645):839–40.

9. Stefanis L. α-Synuclein in Parkinson's Disease. Cold Spring Harbor Perspectives in Medicine [Internet]. 2012;2(2). Available from: /pmc/articles/PMC3281589/ /pmc/articles/PMC3281589/?report=abstract https://www.ncbi.nlm.nih.gov/pmc/articles/PMC3281589/

10. Diao J, Burré J, Vivona S, Cipriano DJ, Sharma M, Kyoung M, et al. Native α-synuclein induces clustering of synaptic-vesicle mimics via binding to phospholipids and synaptobrevin-2/VAMP2. eLife [Internet]. 2013 Aug;2013(2). Available from: https://pubmed.ncbi.nlm.nih.gov/23638301/

11. Choi BK, Choi MG, Kim JY, Yang Y, Lai Y, Kweon DH, et al. Large α-synuclein oligomers inhibit neuronal SNARE-mediated vesicle docking. Proceedings of the National Academy of Sciences of the United States of America. 2013 Aug;110(10):4087–92.

12. Yoo G, Yeou S, Son JB, Shin YK, Lee NK. Cooperative inhibition of SNARE-mediated vesicle fusion by α-synuclein monomers and oligomers. Sci Rep. 2021 May 26;11(1):10955.

13. Bernal-Conde LD, Ramos-Acevedo R, Reyes-Hernández MA, Balbuena-Olvera AJ, Morales-Moreno ID, Argüero-Sánchez R, et al. Alpha-Synuclein Physiology and

Pathology: A Perspective on Cellular Structures and Organelles. Frontiers in Neuroscience [Internet]. 2020 [cited 2023 Sep 13];13. Available from: https://www.frontiersin.org/articles/10.3389/fnins.2019.01399

14. Strohäker T, Jung BC, Liou SH, Fernandez CO, Riedel D, Becker S, et al. Structural heterogeneity of α-synuclein fibrils amplified from patient brain extracts. Nature Communications 2019 10:1. 2019 Aug;10(1):1–12.

15. Ingelsson M. Alpha-Synuclein Oligomers-Neurotoxic Molecules in Parkinson's Disease and Other Lewy Body Disorders. Frontiers in neuroscience [Internet]. 2016 Aug;10(SEP). Available from: https://pubmed.ncbi.nlm.nih.gov/27656123/

16. Emin D, Zhang YP, Lobanova E, Miller A, Li X, Xia Z, et al. Small soluble α-synuclein aggregates are the toxic species in Parkinson's disease. Nature Communications 2022 13:1. 2022 Aug;13(1):1–15.

17. Rockenstein E, Mallory M, Hashimoto M, Song D, Shults CW, Lang I, et al. Differential neuropathological alterations in transgenic mice expressing alpha-synuclein from the platelet-derived growth factor and Thy-1 promoters. Journal of neuroscience research. 2002 Aug;68(5):568–78.

18. Richter F, Stanojlovic M, Käufer C, Gericke B, Feja M. A Mouse Model to Test Novel Therapeutics for Parkinson's Disease: an Update on the Thy1-aSyn ("line 61") Mice. Neurotherapeutics. 2023 Jan;20(1):97–116.

19. Chesselet MF, Richter F, Zhu C, Magen I, Watson MB, Subramaniam SR. A progressive mouse model of Parkinson's disease: the Thy1-aSyn ('Line 61') mice. Neurotherapeutics : the journal of the American Society for Experimental NeuroTherapeutics. 2012 Aug;9(2):297–314.

20. Chartier-Harlin MC, Kachergus J, Roumier C, Mouroux V, Douay X, Lincoln S, et al. Alpha-synuclein locus duplication as a cause of familial Parkinson's disease. Lancet. 2004 Oct 25;364(9440):1167–9.

21. Overk CR, Cartier A, Shaked G, Rockenstein E, Ubhi K, Spencer B, et al. Hippocampal neuronal cells that accumulate α-synuclein fragments are more vulnerable to Aβ oligomer toxicity via mGluR5--implications for dementia with Lewy bodies. Mol Neurodegener. 2014 May 19;9:18.

22. Wrasidlo W, Tsigelny IF, Price DL, Dutta G, Rockenstein E, Schwarz TC, et al. A de novo compound targeting α-synuclein improves deficits in models of Parkinson's disease. Brain. 2016 Dec;139(Pt 12):3217–36.

23. Kim C, Ojo-Amaize E, Spencer B, Rockenstein E, Mante M, Desplats P, et al. Hypoestoxide reduces neuroinflammation and α-synuclein accumulation in a mouse model of Parkinson's disease. J Neuroinflammation. 2015 Dec 18;12:236.

24. Price DL, Koike MA, Khan A, Wrasidlo W, Rockenstein E, Masliah E, et al. The small molecule alpha-synuclein misfolding inhibitor, NPT200-11, produces multiple benefits in an animal model of Parkinson's disease. Sci Rep. 2018 Nov 1;8(1):16165.

25. Subramaniam SR, Vergnes L, Franich NR, Reue K, Chesselet MF. Region specific mitochondrial impairment in mice with widespread overexpression of alpha-synuclein. Neurobiol Dis. 2014 Oct;70:204–13.

26. Rabl R, Breitschaedel C, Flunkert S, Duller S, Amschl D, Neddens J, et al. Early start of progressive motor deficits in Line 61 α-synuclein transgenic mice. BMC Neurosci. 2017 Jan 31;18(1):22.

27. Hong W, Wang Z, Liu W, O'Malley TT, Jin M, Willem M, et al. Diffusible, highly bioactive oligomers represent a critical minority of soluble Aβ in Alzheimer's disease brain. Acta neuropathologica. 2018 Aug;136(1):19.

28. Fertan E, Hung C, Danial JSH, Lam JYL, Preman P, Albertini G, et al. Clearance of beta-amyloid and tau aggregates are size-dependent and altered by an inflammatory challenge. Brain Communications. 2024 Dec 14;fcae454.

29. Hong W, Liu W, Desousa AO, Young-Pearse T, Walsh DM. Methods for the isolation and analysis of Aβ from postmortem brain. Front Neurosci. 2023 Jan 26;17:1108715.

30. Klucken J, Ingelsson M, Shin Y, Irizarry MC, Hedley-Whyte ET, Frosch M, et al. Clinical and biochemical correlates of insoluble alpha-synuclein in dementia with Lewy bodies. Acta Neuropathol. 2006 Feb;111(2):101–8.

31. Frankel S, Sohn R, Leinwand L. The use of sarkosyl in generating soluble protein after bacterial expression. Proc Natl Acad Sci U S A. 1991 Feb 15;88(4):1192–6.

32. Gram H, Theologidis V, Boesen T, Jensen PH. Sarkosyl differentially solubilizes patient-derived alpha-synuclein fibril strains. Frontiers in Molecular Biosciences [Internet]. 2023 [cited 2023 Sep 13];10. Available from: https://www.frontiersin.org/articles/10.3389/fmolb.2023.1177556

33. Fertan E, Böken D, Murray A, Danial JSH, Lam JYL, Wu Y, et al. Cerebral organoids with chromosome 21 trisomy secrete Alzheimer's disease-related soluble aggregates detectable by single-molecule-fluorescence and super-resolution microscopy. Mol Psychiatry. 2023 Dec 15;

34. Danial JSH, Lam JYL, Wu Y, Woolley M, Dimou E, Cheetham MR, et al. Constructing a cost-efficient, high-throughput and high-quality single-molecule localization microscope for super-resolution imaging. Nature protocols. 2022 Aug;17(11):2570–619.

35. Xia Z, Wu Y, Lam JYL, Zhang Z, Burke M, Fertan E, et al. A computational suite for the structural and functional characterization of amyloid aggregates. Cell Reports Methods. 2023 Aug;3(6):100499.

36. Michaels TCT, Yde P, Willis JCW, Jensen MH, Otzen D, Dobson CM, et al. The length distribution of frangible biofilaments. The Journal of Chemical Physics. 2015 Oct 22;143(16):164901.

37. Böken D, Xia Z, Lam JYL, Fertan E, Wu Y, English EA, et al. Ultrasensitive Protein Aggregate Quantification Assays for Neurodegenerative Diseases on the Simoa Platform. Anal Chem. 2024 Dec 24;

38. Böken D, Cox D, Burke M, Lam JYL, Katsinelos T, Danial JSH, et al. Single-Molecule Characterization and Super-Resolution Imaging of Alzheimer's Disease-Relevant Tau Aggregates in Human Samples. Angew Chem Int Ed Engl. 2024 Mar 24;e202317756.

39. Jungmann R, Avendaño MS, Dai M, Woehrstein JB, Agasti SS, Feiger Z, et al. Quantitative super-resolution imaging with qPAINT. Nat Methods. 2016 May;13(5):439–42.

40. Bousset L, Pieri L, Ruiz-Arlandis G, Gath J, Jensen PH, Habenstein B, et al. Structural and functional characterization of two alpha-synuclein strains. Nat Commun. 2013;4:2575.

41. Al-Otaibi N, Aminian J A, Anane RF, Baatsen P, Bakker SE, Bergeron J, et al. Sample preparation in single particle cryo-EM: general discussion. Faraday Discuss. 2022 Nov 8;240(0):81–100.

42. Dirnberger G, Jahanshahi M. Executive dysfunction in Parkinson's disease: a review. J Neuropsychol. 2013 Sep;7(2):193–224.

43. du Plessis S, Bossert M, Vink M, van den Heuvel L, Bardien S, Emsley R, et al. Reward processing dysfunction in ventral striatum and orbitofrontal cortex in Parkinson's disease. Parkinsonism Relat Disord. 2018 Mar;48:82–8.

44. Kobayakawa M, Tsuruya N, Kawamura M. Decision-making performance in Parkinson's disease correlates with lateral orbitofrontal volume. J Neurol Sci. 2017 Jan 15;372:232–8.

45. Braak H, Tredici KD, Rüb U, de Vos RAI, Jansen Steur ENH, Braak E. Staging of brain pathology related to sporadic Parkinson's disease. Neurobiology of Aging. 2003 Mar 1;24(2):197–211.

46. Tinaz S, Courtney MG, Stern CE. Focal cortical and subcortical atrophy in early Parkinson's disease. Mov Disord. 2011 Feb 15;26(3):436–41.

47. Harding AJ, Stimson E, Henderson JM, Halliday GM. Clinical correlates of selective pathology in the amygdala of patients with Parkinson's disease. Brain. 2002 Nov 1;125(11):2431–45.

48. Iljina M, Garcia GA, Horrocks MH, Tosatto L, Choi ML, Ganzinger KA, et al. Kinetic model of the aggregation of alpha-synuclein provides insights into prion-like spreading. Proceedings of the National Academy of Sciences. 2016 Mar;113(9):E1206–15.

49. Cremades N, Cohen SIA, Deas E, Abramov AY, Chen AY, Orte A, et al. Direct Observation of the Interconversion of Normal and Toxic Forms of α-Synuclein. Cell. 2012 May 25;149(5):1048–59.

50. Meisl G, Hidari E, Allinson K, Rittman T, DeVos SL, Sanchez JS, et al. In vivo rate-determining steps of tau seed accumulation in Alzheimer's disease. Science Advances. 2021 Oct 29;7(44):eabh1448.

51. Giguère N, Burke Nanni S, Trudeau LE. On Cell Loss and Selective Vulnerability of Neuronal Populations in Parkinson's Disease. Front Neurol. 2018 Jun 19;9:455.

52. Luna E, Decker SC, Riddle DM, Caputo A, Zhang B, Cole T, et al. Differential α-synuclein expression contributes to selective vulnerability of hippocampal neuron subpopulations to fibril-induced toxicity. Acta Neuropathol. 2018 Jun;135(6):855–75.

53. de Boni L, Watson AH, Zaccagnini L, Wallis A, Zhelcheska K, Kim N, et al. Brain region-specific susceptibility of Lewy body pathology in synucleinopathies is governed by α-synuclein conformations. Acta Neuropathol. 2022 Apr;143(4):453–69.

54. Mahul-Mellier AL, Burtscher J, Maharjan N, Weerens L, Croisier M, Kuttler F, et al. The process of Lewy body formation, rather than simply α-synuclein fibrillization, is one of the major drivers of neurodegeneration. Proc Natl Acad Sci U S A. 2020 Mar 3;117(9):4971–82.

9. Figure captions:

Figure 1. Graphic summary of the experimental design. Line 61 mouse (**a,b**) and post-mortem human brain (**c**) samples were processed by slice soaking, detergent-free pulverised tissue homogenising and from which pellets then sequentially extracted using Triton X-100, and then sarkosyl. Once the soluble aggregates for the respective extraction methods were harvested, the total protein concentration in each sample was measured using a BCA assay (**d**), and the concentration of alpha-synuclein aggregates in the samples were determined using SiMoA (**e**). Then, the size and shape of the alpha-synuclein aggregates were characterised by SiMPull (**f**) and DNA-PAINT imaging (**g**).

Figure 2. Concentration of alpha-synuclein aggregates in the Line 61 mouse brain measured by SiMoA for soaked (**a**), homogenised (**b**), Triton X-100 (**c**), and sarkosyl (**d**) extracted samples and the proportion of the aggregates extracted by the serial processing at 1.5- (**e**), 6- (**f**), 9- (**g**), and 12-months (**h**) of age.

Figure 3. Representative micrographs of super-resolved aggregates from the 12-month-old, Line 61 mouse brain processed by soaking (**a**), homogenising (**b**), Triton X-100 (**c**), and sarkosyl (**d**) extraction (scale bars are 500 nm). Mean alpha-synuclein aggregate cluster length (nm), area (nm^2), and eccentricity for aggregates harvested from the Line 61 mouse brain by soaking (**e, i, m**, respectively), homogenising (**f, j, n**, respectively), Triton X-100 (**g, k, o**, respectively), and sarkosyl (**h, l**, **p**, respectively) extraction.

Figure 4. Cumulative length (nm), area (nm^2), and eccentricity distribution of alpha-synuclein aggregates harvested from Line 61 mouse brain at 1.5-, 6-, 9-, and 12-months of age by soaking (**a, e, i**, respectively), homogenising (**b, f, j**, respectively), Triton X-100 (**c, g, k**, respectively), and sarkosyl (**d, h, l**, respectively) extractions.

Figure 5. Total concentration of alpha-synuclein aggregates in the Line 61 mouse (**a**) and post-mortem human brain (**c**) samples measured by SiMoA for soaking (blue), homogenising (green), Triton X-100 (yellow), and sarkosyl (red) extractions. And total number of localisations measured by DNA-PAINT super-resolution microscopy in the Line 61 (**b**) and post-mortem human brain (**d**) samples, as a measure of total aggregate mass.

Figure 6. Concentration of the alpha-synuclein (αSyn) aggregates extracted by different methods from control (**a**) and PD (**b**) post-mortem human brain samples with SiMoA, and the proportion of the aggregates extracted by the serial processing from the control (**c**) and PD samples (**d**).

Figure 7. Mean alpha-synuclein aggregate cluster length (nm), area (nm^2), and eccentricity for aggregates harvested from the control (**a, d, g**, respectively) and PD (**b, e, h**, respectively) post-mortem human, and 12-month-old Line 61 mouse (**c, f, i**, respectively), harvested by gentle soaking (blue), homogenising (green), Triton X-100 (yellow) and sarkosyl (red) extractions.

Figure 8. Representative micrographs of super-resolved aggregates from the Line 61 mouse model at 12 months of age (**a**), as well as PD (**b**) and control (**c**) post-mortem human, brain samples processed by soaking (cut), homogenising (powder), Triton X-100, and sarkosyl extraction (scale bars are 20 nm).

Figure 9. Fitting of experimental distributions to predictions from simple aggregation model. (a,b) Experimental distribution and best fit of equation (2) for an example distribution from a healthy and a PD sample. All fits are shown in the SI. (c,d) the mean length and relative contribution of the larger distribution to the best fit of the data, for the different extraction methods, comparing healthy and PD samples. (e,f) the mean length and relative contribution of the larger distribution to the best fit of the data, for the different extraction methods, comparing different mouse ages. Error bars are standard errors of the mean across 3 samples.

Supplemental Figure 1. Predicted (above) and fitted (below) length distributions of the alpha-synuclein aggregates with an eccentricity above 0.8 from the control human post-mortem orbitofrontal cortex samples extracted by gentle soaking, homogenising, Triton X-100, and sarkosyl.

Supplemental Figure 2. Predicted (above) and fitted (below) length distributions of the alpha-synuclein aggregates with an eccentricity above 0.8 from the Parkinson's disease human post-mortem orbitofrontal cortex samples extracted by gentle soaking, homogenising, Triton X-100, and sarkosyl.

Supplemental Figure 3. Predicted (above) and fitted (below) length distributions of the alpha-synuclein aggregates with an eccentricity above 0.8 from the Line 61 mouse brain samples at 1.5 months of age, extracted by gentle soaking, homogenising, Triton X-100, and sarkosyl extractions.

Supplemental Figure 4. Predicted (above) and fitted (below) length distributions of the alpha-synuclein aggregates with an eccentricity above 0.8 from the Line 61 mouse brain samples at 6 months of age, extracted by gentle soaking, homogenising, Triton X-100, and sarkosyl extractions.

Supplemental Figure 5. Predicted (above) and fitted (below) length distributions of the alpha-synuclein aggregates with an eccentricity above 0.8 from the Line 61 mouse brain samples at 9 months of age, extracted by gentle soaking, homogenising, Triton X-100, and sarkosyl extractions.

Supplemental Figure 6. Predicted (above) and fitted (below) length distributions of the alpha-synuclein aggregates with an eccentricity above 0.8 from the Line 61 mouse brain samples at 6 months of age, extracted by gentle soaking, homogenising, Triton X-100, and sarkosyl extractions.

Figure 1

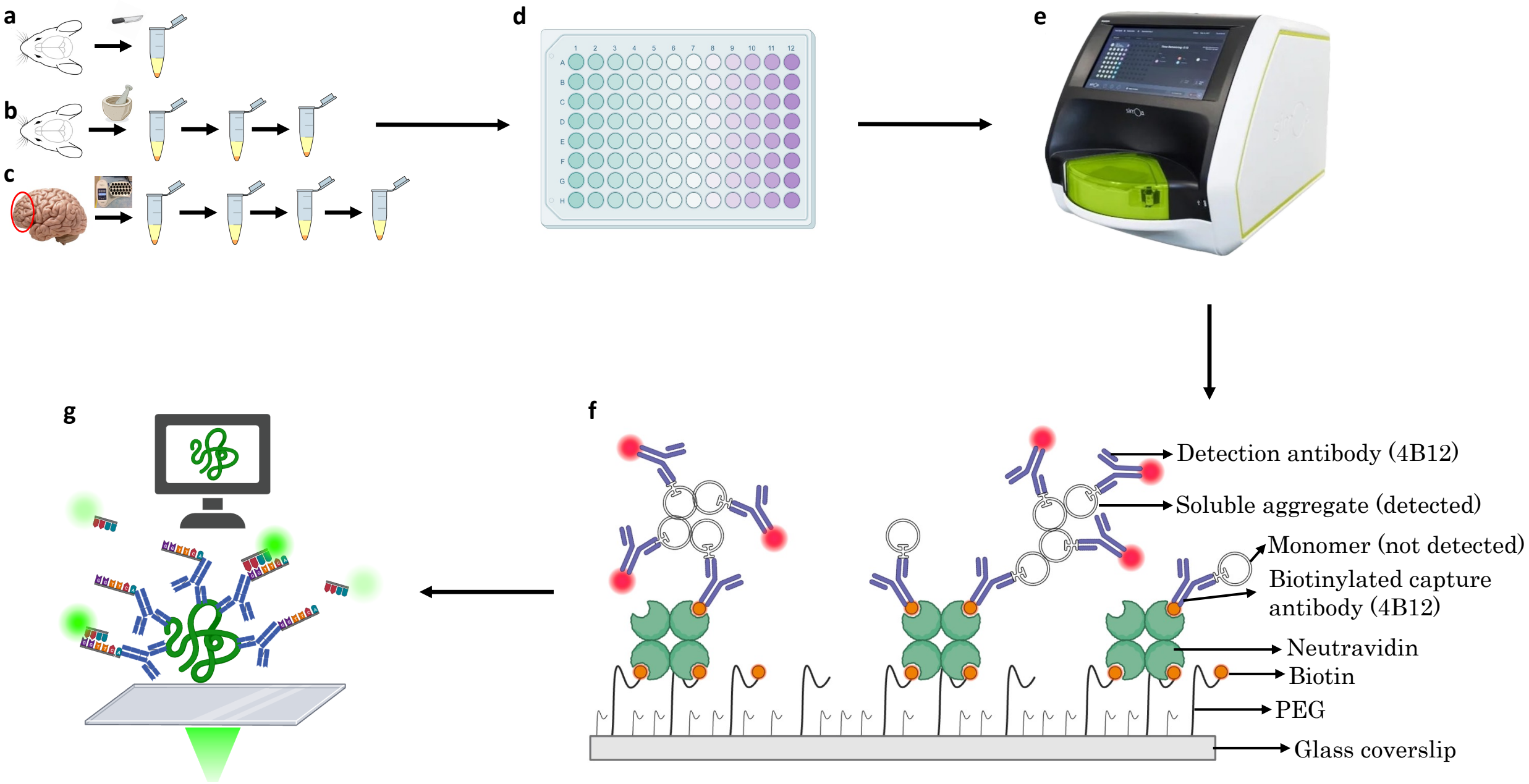
a
b
c
d
e
f
g
Detection antibody (4B12)
Soluble aggregate (detected)
Monomer (not detected)
Biotinylated capture antibody (4B12)
Neutravidin
Biotin
PEG
Glass coverslip

Figure 2

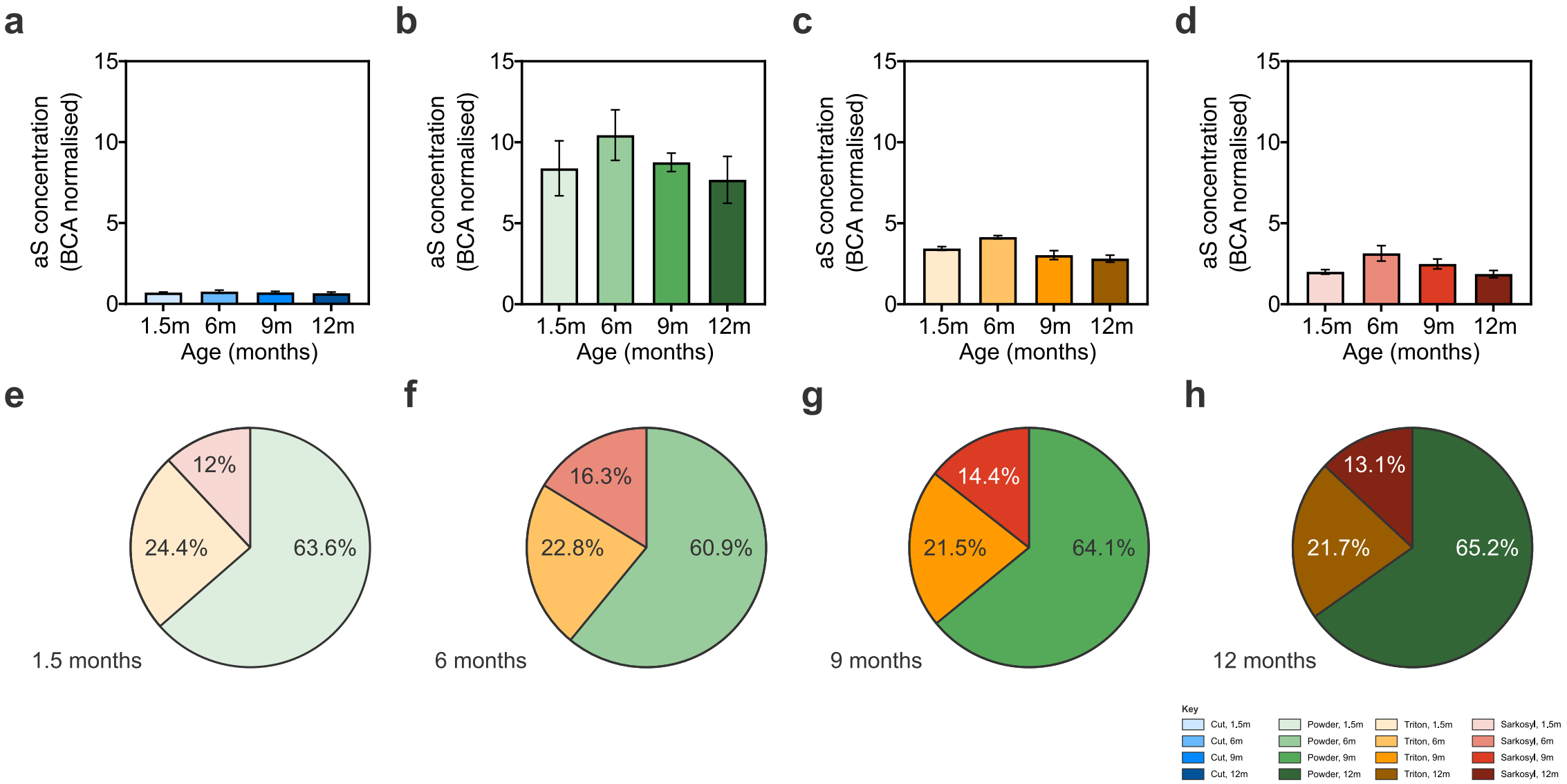
a
b
c
d
aS concentration (BCA normalised)
15
10
5
0
1.5m
6m
9m
12m
Age (months)
e
12%
24.4%
63.6%
1.5 months
f
16.3%
22.8%
60.9%
6 months
g
14.4%
21.5%
64.1%
9 months
h
13.1%
21.7%
65.2%
12 months
Key
Cut, 1.5m
Cut, 6m
Cut, 9m
Cut, 12m
Powder, 1.5m
Powder, 6m
Powder, 9m
Powder, 12m
Triton, 1.5m
Triton, 6m
Triton, 9m
Triton, 12m
Sarkosyl, 1.5m
Sarkosyl, 6m
Sarkosyl, 9m
Sarkosyl, 12m

Figure 3

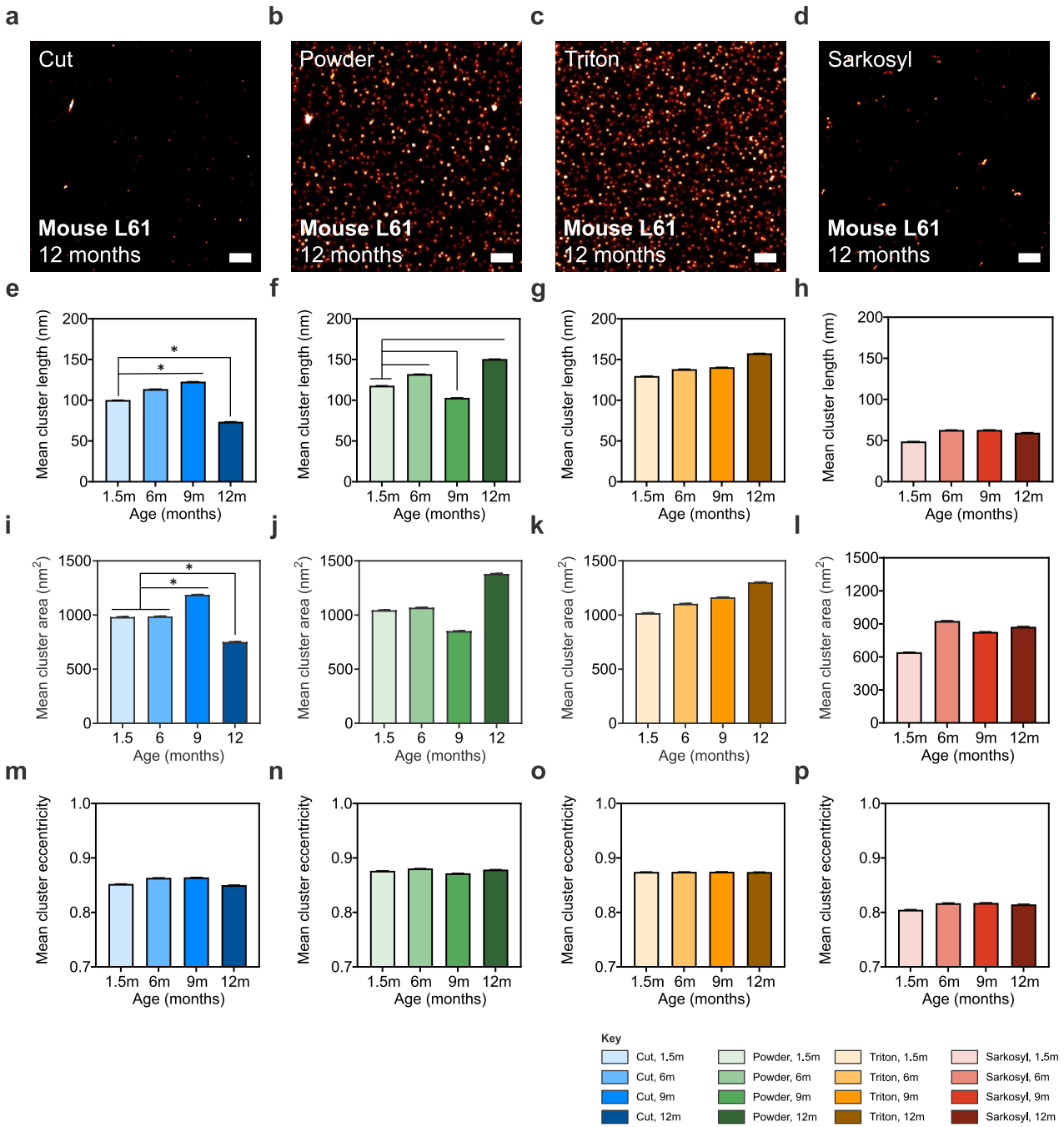
a
Cut
Mouse L61
12 months
b
Powder
Mouse L61
12 months
c
Triton
Mouse L61
12 months
d
Sarkosyl
Mouse L61
12 months
e
f
g
h
Mean cluster length (nm)
Age (months)
1.5m 6m 9m 12m
i
j
k
l
Mean cluster area (nm²)
Age (months)
1.5 6 9 12
m
n
o
p
Mean cluster eccentricity
Age (months)
Key
Cut, 1.5m
Cut, 6m
Cut, 9m
Cut, 12m
Powder, 1.5m
Powder, 6m
Powder, 9m
Powder, 12m
Triton, 1.5m
Triton, 6m
Triton, 9m
Triton, 12m
Sarkosyl, 1.5m
Sarkosyl, 6m
Sarkosyl, 9m
Sarkosyl, 12m

Figure 4

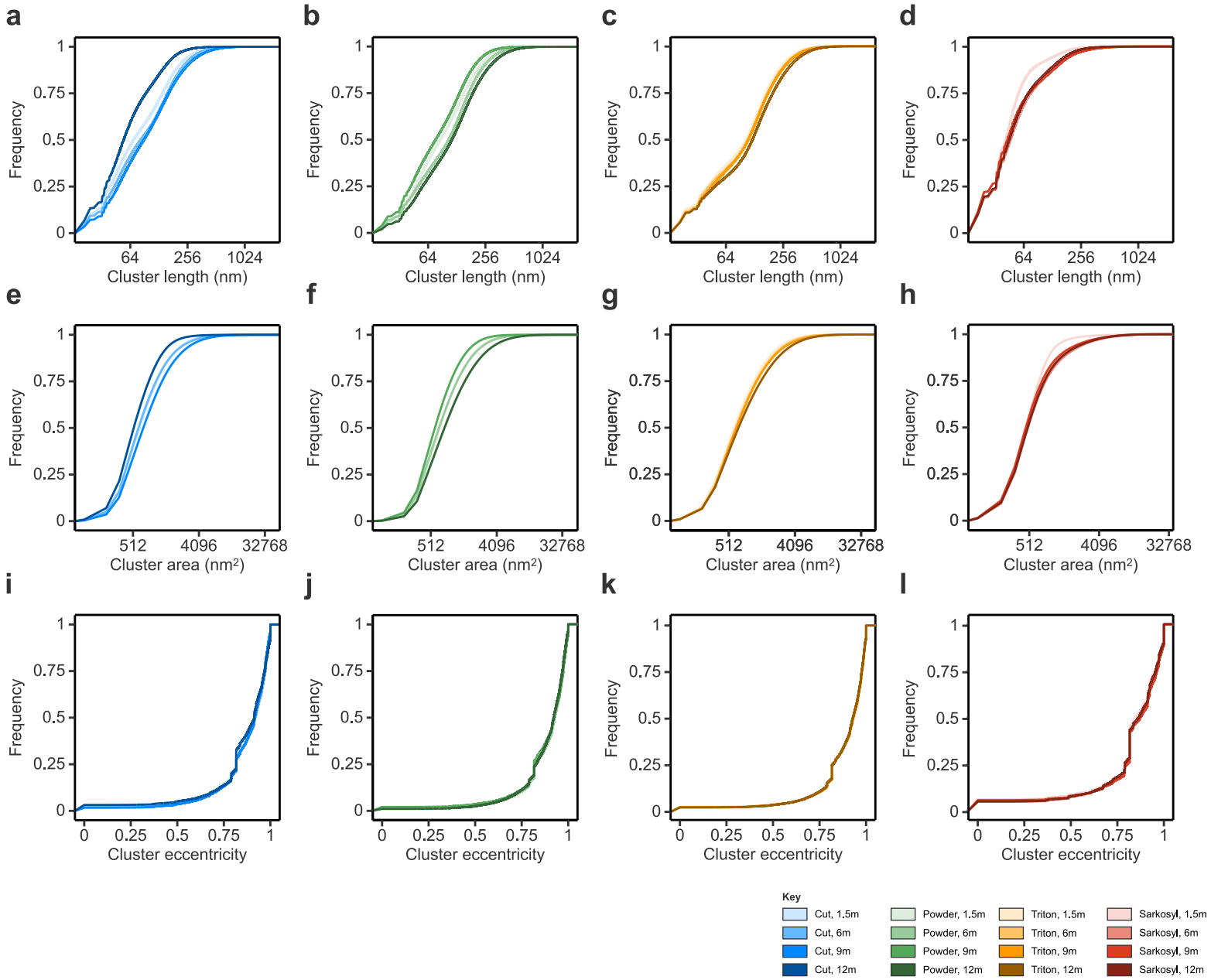
a
b
c
d
e
f
g
h
i
j
k
l
Frequency
Cluster length (nm)
Cluster area (nm²)
Cluster eccentricity
Key
Cut, 1.5m
Cut, 6m
Cut, 9m
Cut, 12m
Powder, 1.5m
Powder, 6m
Powder, 9m
Powder, 12m
Triton, 1.5m
Triton, 6m
Triton, 9m
Triton, 12m
Sarkosyl, 1.5m
Sarkosyl, 6m
Sarkosyl, 9m
Sarkosyl, 12m

Figure 5

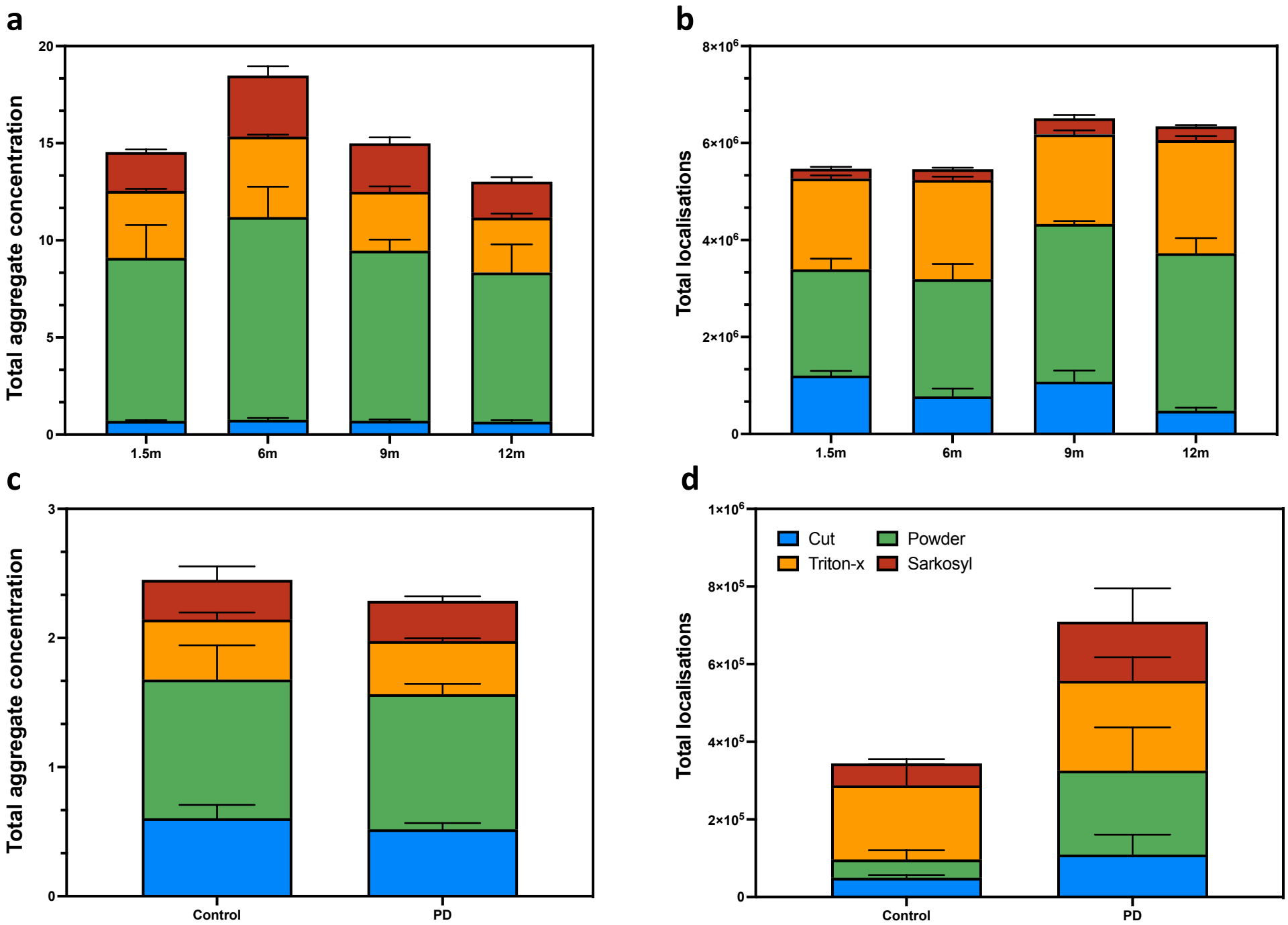
a
Total aggregate concentration
20
15
10
5
0
1.5m
6m
9m
12m
b
Total localisations
8×10^6
6×10^6
4×10^6
2×10^6
0
1.5m
6m
9m
12m
c
Total aggregate concentration
3
2
1
0
Control
PD
d
Total localisations
1×10^6
8×10^5
6×10^5
4×10^5
2×10^5
0
Cut
Powder
Triton-x
Sarkosyl
Control
PD

Figure 6

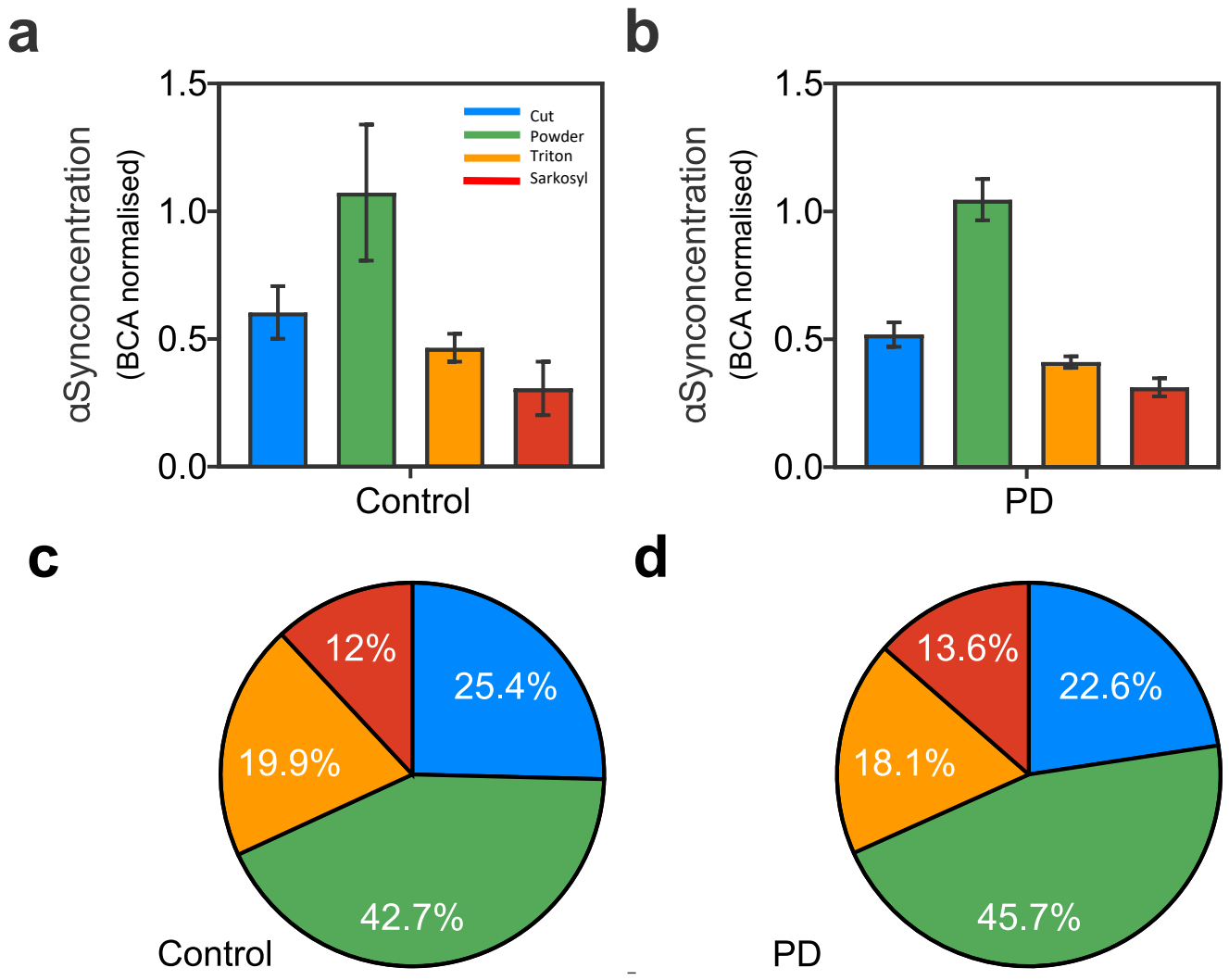
a
b
c
d
αSynconcentration
(BCA normalised)
1.5
1.0
0.5
0.0
Cut
Powder
Triton
Sarkosyl
Control
PD
12%
25.4%
19.9%
42.7%
Control
13.6%
22.6%
18.1%
45.7%
PD

Figure 7

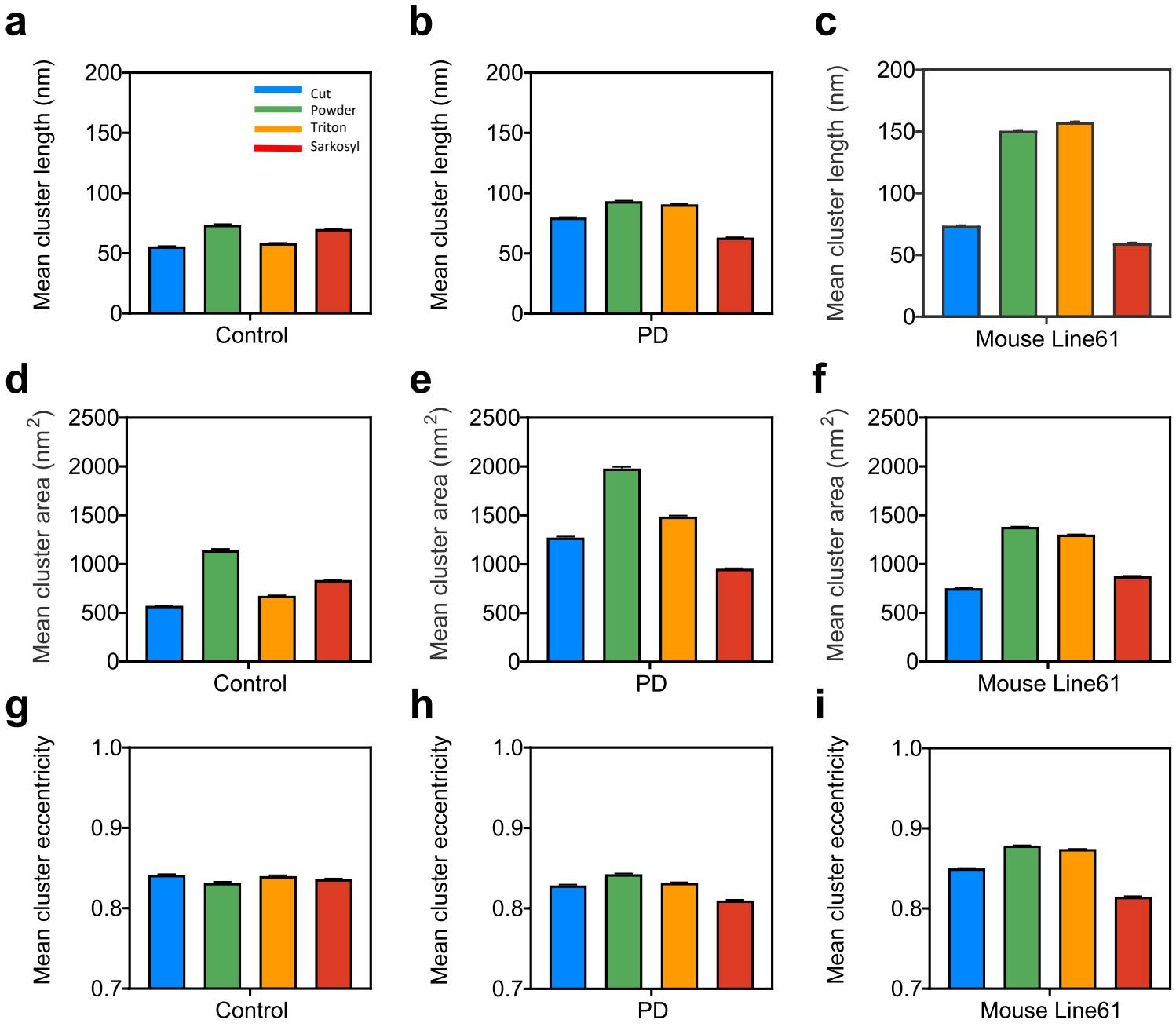
a
b
c
d
e
f
g
h
i
Mean cluster length (nm)
Mean cluster area (nm2)
Mean cluster eccentricity
Cut
Powder
Triton
Sarkosyl
Control
PD
Mouse Line61
200
150
100
50
0
2500
2000
1500
1000
500
1.0
0.9
0.8
0.7

Figure 8

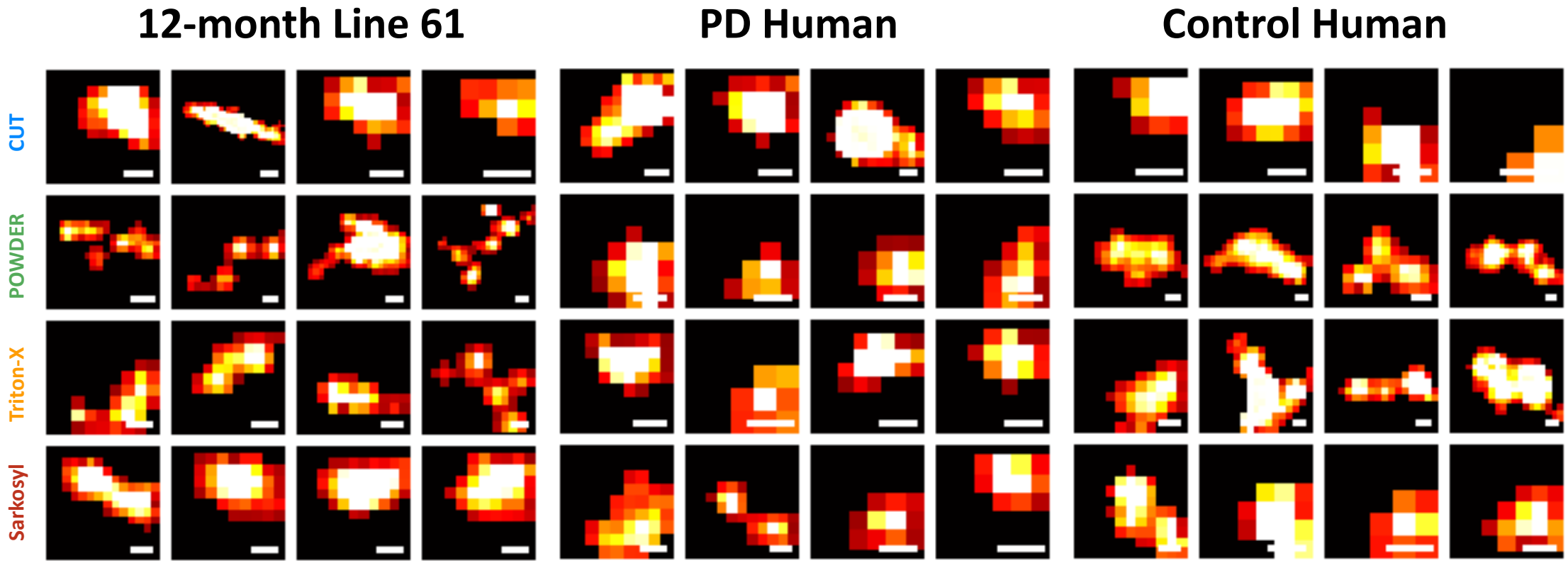
12-month Line 61
PD Human
Control Human
CUT
POWDER
Triton-X
Sarkosyl

Figure 9

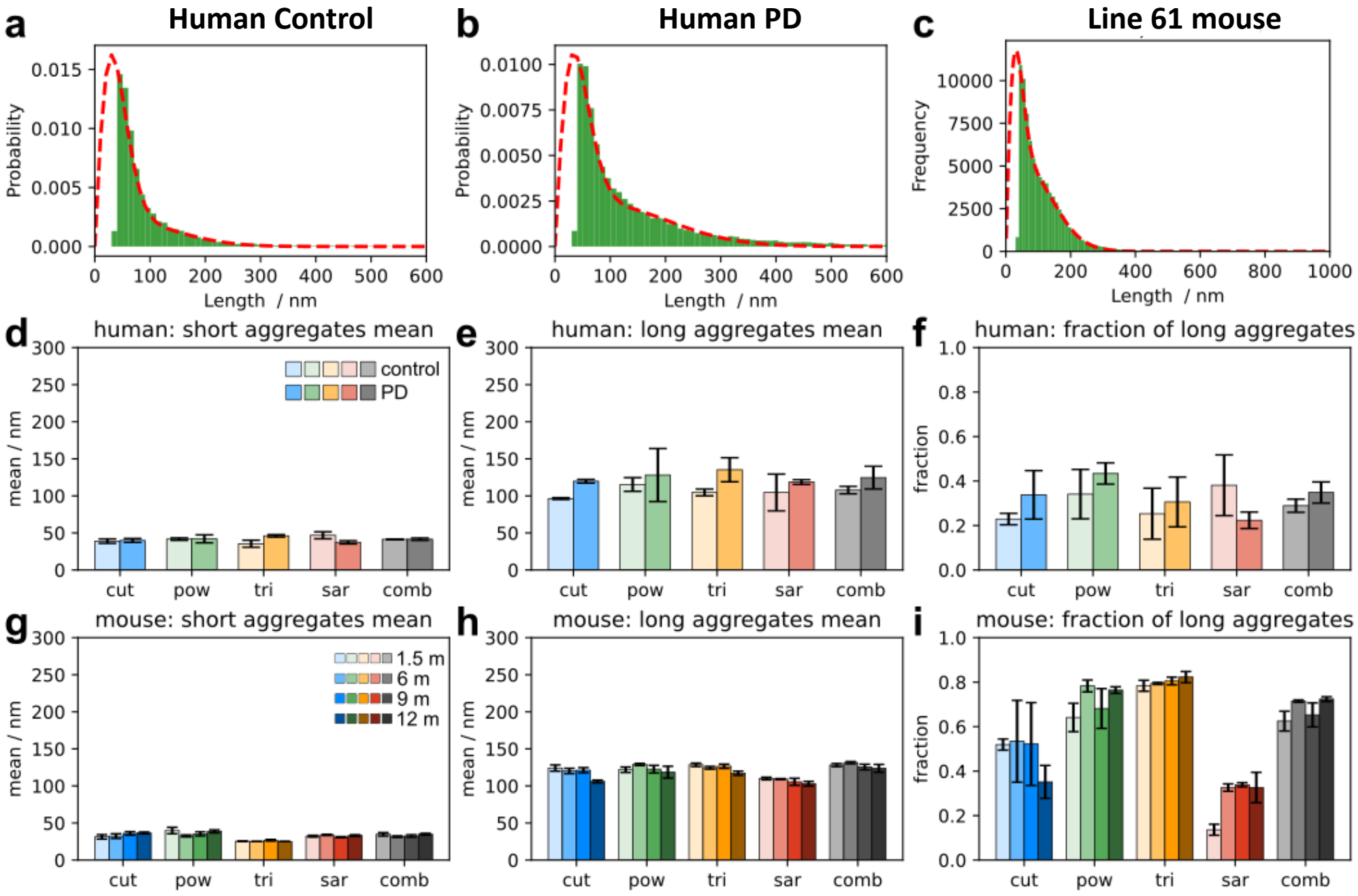
a
Human Control
Probability
Length / nm
b
Human PD
Probability
Length / nm
c
Line 61 mouse
Frequency
Length / nm
d
human: short aggregates mean
control
PD
mean / nm
cut
pow
tri
sar
comb
e
human: long aggregates mean
mean / nm
f
human: fraction of long aggregates
fraction
g
mouse: short aggregates mean
1.5 m
6 m
9 m
12 m
mean / nm
h
mouse: long aggregates mean
mean / nm
i
mouse: fraction of long aggregates
fraction

Table 1. Demographic data for human orbitofrontal cortex tissue samples.

Case	Diagnosis	Braak stage	Sex	Age
BB19.0032/NP19.108	PD	4	Female	86
BB19.0010/NP19.023	PD	4	Female	78
BB16.0014/NP16.162	PD	5	Male	74
NP16.164/BB16.16	Control	0	Male	70
NP16.284/BB16.40	Control	0	Female	70
NP16.239/BB16.026	Control	0	Female	82